Soft Matter

PAPER

Cite this: *Soft Matter*, 2015, **11**, 4742

Heterogeneous flow kinematics of cellulose nanofibril suspensions under shear

F. Martoïa,[abcde] C. Perge,[f] P. J. J. Dumont,*[abc] L. Orgéas,[de] M. A. Fardin,[f] S. Manneville[f] and M. N. Belgacem[abc]

Received 5th March 2015,
Accepted 9th April 2015

DOI: 10.1039/c5sm00530b

www.rsc.org/softmatter

The rheology of NFC suspensions that exhibited different microstructures and colloidal stability, namely TEMPO and enzymatic NFC suspensions, was investigated at the macro and mesoscales using a transparent Couette rheometer combined with optical observations and ultrasonic speckle velocimetry (USV). Both NFC suspensions showed a complex rheology, which was typical of yield stress, non-linear and thixotropic fluids. Hysteresis loops and erratic evolutions of the macroscale shear stress were also observed, thereby suggesting important mesostructural changes and/or inhomogeneous flow conditions. The *in situ* optical observations revealed drastic mesostructural changes for the enzymatic NFC suspensions, whereas the TEMPO NFC suspensions did not exhibit mesoscale heterogeneities. However, for both suspensions, USV measurements showed that the flow was heterogeneous and exhibited complex situations with the coexistence of multiple flow bands, wall slippage and possibly multidimensional effects. Using USV measurements, we also showed that the fluidization of these suspensions could presumably be attributed to a progressive and spatially heterogeneous transition from a solid-like to a liquid-like behavior. As the shear rate was increased, the multiple coexisting shear bands progressively enlarged and nearly completely spanned over the rheometer gap, whereas the plug-like flow bands were eroded.

1 Introduction

Cellulose nanofibrils (NFCs) are the main reinforcing constituents of plant cell walls. They can be extracted from cellulosic fibers by mechanical and/or chemical processing routes in the form of aqueous colloidal suspensions. Because of their intrinsic outstanding mechanical properties[1–3] (Young's Modulus $E \approx 80$ GPa and ultimate tensile stress $\sigma \approx 1$ GPa) and their reactive surface chemistry, NFCs constitute attractive renewable nanoscale fibrous reinforcements for several applications. They can be used in cosmetics as gelling agents or in the papermaking industry as coating to reinforce or to functionalize substrates[4] or even as transparent films/nanopapers for packaging.[5,6] They are also used as slender nano-reinforcements in polymer matrix composites[7,8] that have been in development in the last ten years. Understanding the rheology of NFC suspensions is crucial either to fully exploit the end-use properties or to optimize the forming processes of the aforementioned materials, and more precisely the placement of the nanoscale fibrous reinforcements.[9]

To reduce energy demand during the NFC extraction processes and to make these processes more environmentally friendly, enzymatic or oxidation pre-treatments are used prior to mechanical treatments. Enzymatic treatment[10,11] consists of a mild hydrolysis of cellulosic fibers, whereas TEMPO oxidation[12–14] is a chemical modification of hydroxyl groups (–OH) at the surface of the microfibrils into carboxylate ones ($–COO^-$). Depending on the extraction processes, the morphology as well as the physico-chemical surface properties of NFCs are different. NFC suspensions produced by mechanical disintegration with or without enzymatic pre-treatment are polydisperse suspensions,[15,16] *i.e.*, they contain both microscale elements such as partially fibrillated cellulose fibers but also nanoscale elements in the form of elementary fibrils or bundles of fibrils with a diameter that ranges between 5 and 100 nm and a length that ranges between 1 and 10 μm.[17] Because of the low surface charge of the native extracted cellulose nanofibrils (zeta potential $\xi \approx -15$ mV), mechanical and enzymatic NFC suspensions often exhibit flocs whose size ranges between 50 μm and 1000 μm and exhibit opaque textures even at very low NFC concentrations.[18,19] TEMPO NFC suspensions are less polydisperse suspensions[13,20] and contain a few fibril bundles and mostly individualized fibrils having a diameter ranging from 3 to 6 nm and a length from 1 to 2 μm.

[a] *Univ. Grenoble Alpes, LGP2, F-38000 Grenoble, France. E-mail: pierre.dumont@grenoble-inp.fr*
[b] *CNRS, LGP2, F-38000 Grenoble, France*
[c] *Agefpi, LGP2, F-38000 Grenoble, France*
[d] *Univ. Grenoble Alpes, 3SR, F-38000 Grenoble, France*
[e] *CNRS, 3SR, F-38000 Grenoble, France*
[f] *Laboratoire de Physique – ENS de Lyon, CNRS UMR 5672, 46 Allée d'Italie, 69364 Lyon cedex 07, France*

These suspensions are commonly much more transparent and are not flocculated because of their more homogenous structures that contain small highly charged slender nanoparticles (zeta potential $\xi \approx -50$ mV).[13]

Regardless of the extraction routes, the rheology of NFC suspensions is complex, poorly characterized and still not well understood and modeled, which limits the use of NFCs. At the macroscale, *i.e.*, at the rheometer scale, mechanical, enzymatic or TEMPO NFC suspensions are commonly regarded as thixotropic yield stress fluids.[21] These suspensions exhibit a macroscale yield stress $\bar{\tau}_0$ at low macroscale shear rates $\left(0.001\ \mathrm{s}^{-1} \leq \bar{\dot{\gamma}} \leq 0.1\ \mathrm{s}^{-1}\right)$ and a shear thinning behavior at higher shear rates[22–24] $\left(10\ \mathrm{s}^{-1} \leq \bar{\dot{\gamma}} \leq 1000\ \mathrm{s}^{-1}\right)$. In addition, at intermediate shear rates $\left(0.1\ \mathrm{s}^{-1} \leq \bar{\dot{\gamma}} \leq 10\ \mathrm{s}^{-1}\right)$, several studies[18,24–26] reported macroscale rheograms $\bar{\tau}\left(\bar{\dot{\gamma}}\right)$ with the presence of hysteresis regions with shear stress plateaus. At the mesoscale, *i.e.*, at sizes above or of the order of the representative volume of the suspensions, *i.e.*, approximately five to ten NFC lengths, the rheology is complex and strongly affected by the extraction process.[27] By investigating the shear rheology of enzymatic suspensions with a combination of a rotational dynamic rheometer and digital imaging techniques, several authors[18,25] reported the presence of flocculated structures in enzymatic NFC suspensions. The complex aggregation–disaggregation kinetics of flocs was correlated with the complex macroscale rheograms recorded at intermediate and high shear rates. Surprisingly, the rheology of TEMPO NFC suspensions for which NFCs are electrostatically stabilized by the presence of carboxylate groups at their surface has been less investigated. The shear rheology of these suspensions was mainly studied in the ''stationary state'' and in a narrow shear rate range.[23,28]

Although this point has not yet been deeply discussed in the literature,[19,21,29,30] the complex macroscale shear rheology of NFC suspensions may be related to rheometry problems that are often reported while shearing other yield stress fluids:[31–35] wall slippage resulting from the geometric characteristics of rheometers (*e.g.* under non-ideal boundary conditions), mesoscale flow heterogeneities such as shear strain localization, shear banding or other material heterogeneities such as migration–segregation. For example, when subjected to shear flow, soft glassy materials (clay suspensions, concentrated emulsions, colloidal gels) exhibit a variety of complex rheological behaviors because the applied shear strain may disrupt and rearrange the microstructure over a wide range of spatial and temporal scales leading to heterogeneous flow properties.[34,36,37] More particularly, in thixotropic yield stress fluids such as in colloidal suspensions, the coexistence of two phenomena in competition, *i.e.*, a shear-induced rejuvenation or destructuration and an aging-induced restructuration, leads to heterogeneous flows such as shear banding. All the aforementioned problems hinder proper assessment of the ''true'' rheology, and are often the source of complex macroscale rheograms, showing for example the presence of stress minimum in flow curves[38] or complex hysteresis loops[39,40] when measurements are performed by sweeping up then down (or *vice versa*) the apparent shear rate. It is also important to note that in the case of semi-flexible slender fiber suspensions as for example in carbon nanotube suspensions[41] or even in non-colloidal glass fiber suspensions,[42] the flow may reorient and deform (bend, stretch) the particles, which also leads to complex flow properties.

To overcome the aforementioned rheometry difficulties, proper rheometry techniques have to be used. For instance, the use of rheometers coupled with 2D surface and bulk visualization setups[25,38] (a transparent measuring cell) enables a link between complex macroscale rheology and mesoscale heterogeneous flows to be experimentally established. However, even if these techniques are extremely informative, they cannot provide local velocity measurements, so that the ''true'' rheology of the material cannot be precisely estimated from the global rheological data.

To better understand the local flow behavior of many complex fluids, several rheometry setups dedicated to local velocity measurements have recently emerged.[32] A first approach, the so called Particle Imaging Velocimetry[43] (PIV), consists of adding particles to the investigated fluid and measuring their displacements using optical microscopy or laser sheet techniques. Unfortunately, these techniques can only be used for transparent fluids. Other advanced rheometry setups based on Magnetic Resonance Imaging[41,44,45] (MRI) or high frequency Ultrasonic Speckle Velocimetry[46,47] (USV) enable space and time-resolved velocity profiles to be measured for a wide range of fluids. In addition, rheometry setups based on scattered-radiation methods[48] (Small Angle X-rays Scattering SAXS, Small Angle Neutron Scattering SANS, Static Light Scattering SLS) can provide a multiscale space and time-resolved description of the structure of the sheared materials. Note that none of the aforementioned techniques has already been used to study the rheology of NFCs.

Thus, the objectives of this study were (i) to experimentally investigate the shear rheology of colloidal enzymatic and TEMPO NFC water suspensions, (ii) to describe the temporal and spatial heterogeneities that were encountered during rheological testing, and (iii) to outline the potential mesostructural and microstructural origins of the observed flow phenomena.

Bearing in mind the aforementioned difficulties, two types of techniques were used to investigate the rheology of these suspensions while sweeping down and then up the applied macroscopic shear rate, and *vice versa.* First, a transparent Couette rheometer enabled potential flow-induced mesostructural changes to be observed. In addition, the use of an ultrasonic speckle velocimetry (USV) setup enabled two-dimensional time-resolved characterization of the mesoscale flow of the considered suspensions, *i.e.*, the evolution of the local velocity field within the Couette cell.

2 Materials and experimental procedures

2.1 Extraction of NFCs

Enzymatic and TEMPO NFCs were extracted from a commercial bleached eucalyptus kraft pulp (Celbi, Portugal) following the two extraction routes shown in Fig. 1. The used bleached

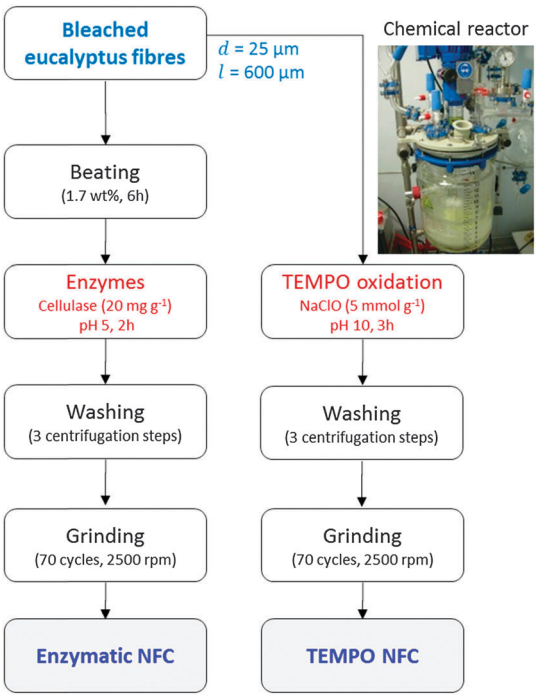

Fig. 1 Simplified scheme of the two extraction routes used for obtaining enzymatic and TEMPO NFC suspensions.

eucalyptus fibers have a mean diameter of 25 µm and a mean length of 600 µm. For the enzymatic NFCs, fibers in water suspension (1.7 wt%) were first refined using a Valley beater for 6 h and then hydrolyzed under mild conditions by adding 20 mg of enzymes per gram of fibers (Celluclast ATCC 26921, Sigma-Aldrich, France). The ensuing suspension was then maintained at pH 5 using a 0.8 M acetate buffer solution at a temperature of 50 °C for 2 h. In the case of the TEMPO treatment, fibers were first oxidized by the addition of 5 mmol of NaClO per gram of fibers in the presence of TEMPO (0.1 mmol per gram of fibers) and NaBr (1 mmol per gram of fibers) catalysts at pH 10 for 3 h. To remove all chemicals, enzyme and TEMPO treated fibers were then centrifuged three times at 10 000 rpm for 10 min and redispersed three times using a homogenizer (Ultra Turrax T65, IKA, France) at 15 000 rpm for 30 s. Suspensions were at pH ranging from 7 to 8 after this operation and were then fibrillated 70 times through a grinder (model MKCA6-2, disk model MKGA6-80#, Masuko Sangyo Co. Ltd, Japan) revolving at a rotation speed of 2500 rpm and with a clearance gauge of 0.

2.2 Morphology of processed NFCs

The morphology of NFCs was investigated using an optical microscope (Axio imager M1m, Zeiss) and an atomic force microscope (AFM, Nanoscope III, Veeco, Canada). The qualitative study of the microstructure revealed that enzymatic NFC suspensions were polydisperse suspensions containing (i) partially fibrillated eucalyptus fibers (diameter ≈ 20 µm and length ≈ 250 µm, see Fig. 2a), (ii) bundles of fibrils having a diameter ranging between 100 and 500 nm, and (iii) nanoscale elements in the form of individualized fibrils with a diameter ranging from 20 to 50 nm.

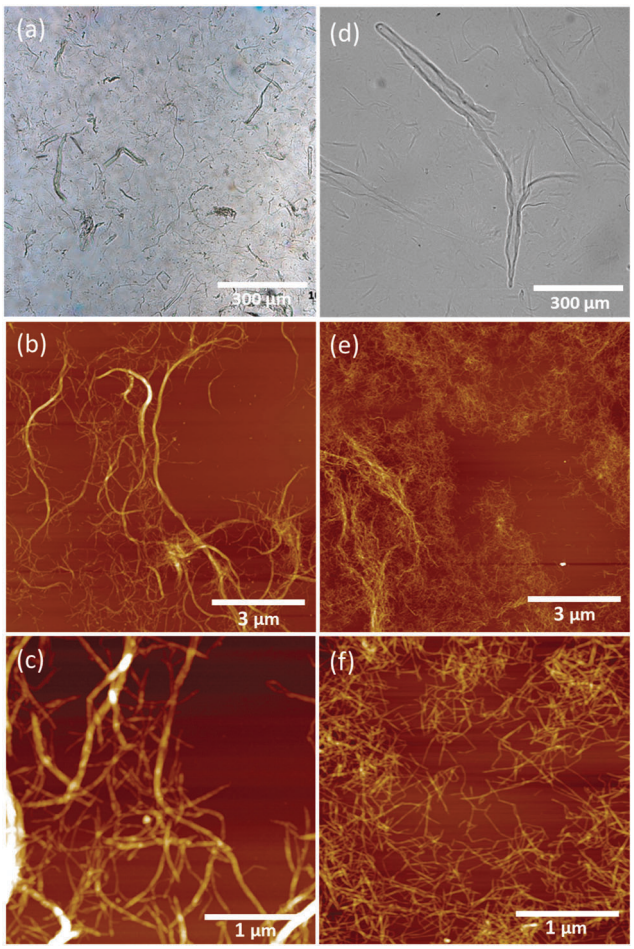

Fig. 2 Light optical micrographs of (a) enzymatic NFCs and (d) TEMPO NFCs in suspension at 0.1 wt%. AFM micrographs of (b, c) enzymatic NFC films, and (e, f) TEMPO NFC films obtained after drying the suspensions diluted at 0.001 wt%.

The isolated NFCs shown in Fig. 2b had lengths that ranged between 1 and 10 µm. However, note that a more precise determination of the length distribution of these very polydisperse suspensions still remains a challenging problem.

In contrast, TEMPO NFC suspensions were much less polydisperse, as they exhibited a few fibers close to their original dimensions (see Fig. 2d) and very small slender individualized fibrils with a diameter and length ranging between 3 and 6 nm and between1 and 1.5 µm, respectively (Fig. 2e and f).

The content of carboxyl groups (–COOH) Γ_{NFC} determined by conductometric titration was 0.05 mmol g^{-1} for enzymatic NFCs (close to the value obtained for bleached eucalyptus fibers), whereas this content was 1.45 mmol g^{-1} for NFCs obtained after TEMPO-mediated oxidation. Thus, TEMPO NFCs were much more electrically charged and stable in water suspension.

2.3 Rheometry

2.3.1 Taylor–Couette rheometry. The rheology of NFC suspensions was first studied using a stress-controlled rheometer (ARG2, TA Instruments) equipped with a transparent Taylor–Couette cell of height H = 60 mm (inner polished PEEK rotating

cylinder of radius R_1 = 23 mm, fixed sand-blasted PMMA stator of radius R_2 = 25 mm, gap $e = R_2 - R_1$ = 2 mm), which enabled potential macro and mesoscale flocs or flow heterogeneities to be observed while shearing the NFC suspensions. The photographs were taken every 5 s using a 36.2 megapixels camera (Nikon D800) equipped with a 100 mm macro lens, the observed zone being illuminated with two LED light sources positioned at ±90°. All the measurements were performed at 20 °C using suspensions that were pre-sheared at 1000 s^{-1} for 60 s. A solvent trap was also systematically used to prevent water evaporation.

From the imposed rotor rotation velocity Ω around the $\mathbf{e}_z$-direction and the measured reaction torque Γ, and assuming a homogeneous flow in a gap e sufficiently small compared to R_1, the rheograms showing the macroscale shear stress:

$$\bar{\tau} = \frac{{R_1}^2 + {R_2}^2}{4\pi H {R_1}^2 {R_2}^2}\Gamma. \quad (1)$$

as a function of the macroscale shear rate $\bar{\dot{\gamma}}$:

$$\bar{\dot{\gamma}} = \frac{{R_1}^2 + {R_2}^2}{{R_2}^2 - {R_1}^2}\Omega \quad (2)$$

were obtained by decreasing $\bar{\dot{\gamma}}$ from 1000 to 0.001 s^{-1} in 45 logarithmically-spaced steps of duration δ_t = 50 s and then by increasing $\bar{\dot{\gamma}}$ over the same range, and *vice versa*.

2.3.2 Ultrasonic speckle velocimetry (USV) rheometry. Rheo-ultrasonic velocimetry (rheo-USV) measurements were performed using the same measuring Taylor–Couette cell which was immersed in a large water tank (total volume 2.2 l) connected to a water bath thermostat (230-CCNR Huber Ministat) maintaining a test temperature of 20 °C and providing proper acoustic coupling with a fair impedance matching between the sample contained in the cell and the ultrasonic transducer array (see Fig. 3). A detailed explanation of the rheo-USV setup is given elsewhere.[46] In short, the heterogeneous structure of the NFC suspensions under study scatters high-frequency ultrasound (15 MHz in the present case) efficiently enough to allow for ultrasonic images to be recorded with a custom-made ultrafast scanner.[46] Velocity maps within a vertical cross-section of the Taylor–Couette cell are obtained by cross-correlating successive ultrasonic images of the NFC suspensions.

More precisely, as sketched in Fig. 3, our rheo-ultrasonic setup enables the projection $v_y(x,y,z,t)$ of the velocity vector $\mathbf{v}(\mathbf{x},t) = v_x\mathbf{e}_x + v_y\mathbf{e}_y + v_z\mathbf{e}_z = v_r\mathbf{e}_r + v_\theta\mathbf{e}_\theta + v_z\mathbf{e}_z$ of mesoscale points flowing at a position $\mathbf{x} = x\mathbf{e}_x + y\mathbf{e}_y + z\mathbf{e}_z = r\mathbf{e}_r + z\mathbf{e}_z$ to be recorded along the ultrasonic propagation direction $\mathbf{e}_y$ over a region of interest (centered in the total height H of the cell) which had a height h = 32 mm, a width $e' \approx e$ = 2 mm and a thickness t = 300 μm, simultaneously with macroscopic rheological data. In the following sections, the time-space velocity maps have a spatial resolution of 70 μm along r and of 250 μm along z as well as a time resolution of 0.5 s. By noting $\varphi = (\widehat{\mathbf{e}_r, \mathbf{e}_y})$ the inclination angle of the ultrasonic transmitters–receivers with respect to the mean radial direction of the region of interest (φ = 5°, see Gallot *et al.*[46] for the calibration procedure), v_y can

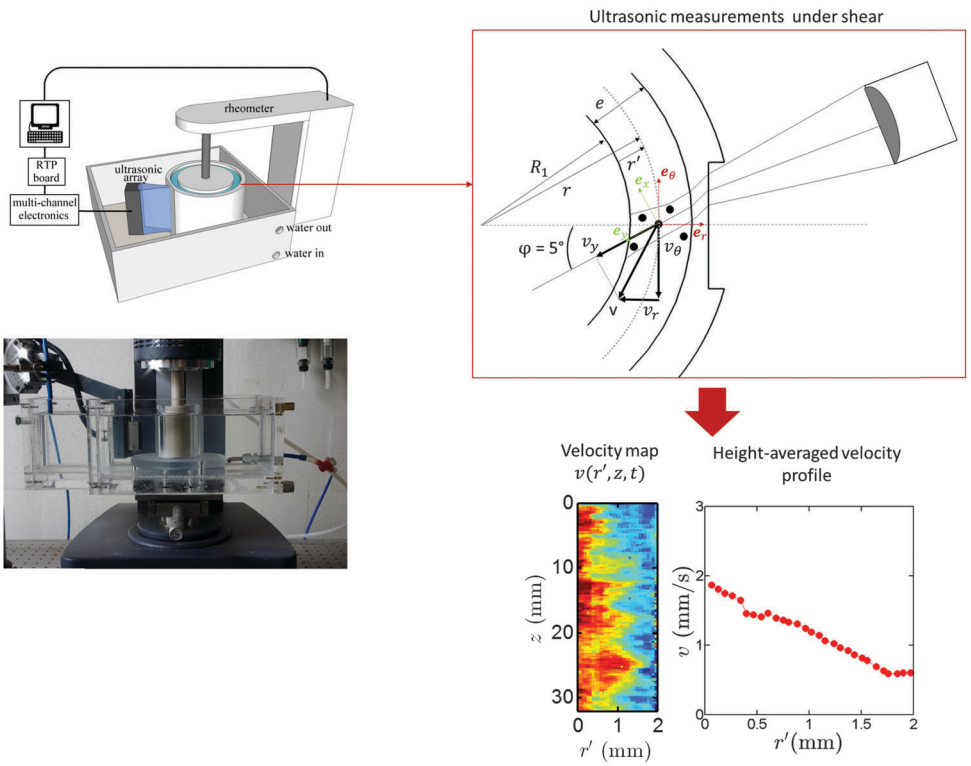

Fig. 3 Schematic presentation of the ultrafast ultrasonic speckle velocimetry (USV) setup from the Taylor–Couette cell used (top left) to the velocity map $v(r',z,t)$ given in eqn (4) and the height-averaged velocity profile obtained during the shear test (bottom right). Note also that in this sketch, the rotor is located at r' = 0 mm and the stator at r' = 2 mm.

be expressed as a function of radial v_r and orthoradial v_θ components of $\mathbf{v}$ as follows (see Fig. 3):

$$v_y = v_r \cos\varphi + v_\theta \sin\varphi. \quad (3)$$

The use of a small incident angle φ and a narrow gap e leads to a low variation of the θ angle across the ultrasonic propagation direction $\mathbf{e}_y$ (see Fig. 3), so that, all the velocity profiles presented in this study mainly correspond to the velocity $v(r',z)$ calculated from the ratio $\frac{v_y(y,z)}{\sin\varphi}$ as follows:

$$v(r',z) = \frac{v_y(y,z)}{\sin\varphi} \simeq v_\theta(r',z) + \frac{v_r(r',z)}{\tan\varphi}. \quad (4)$$

It is worth noting that under these conditions, the use of the USV technique does not allow the orthoradial component v_θ to be measured independently of the radial component v_r, and does not provide any information on the presence of a vertical component v_z in the vorticity direction. However, the information gathered by this technique, *i.e.*, the velocity maps and profiles (see Fig. 3) and their temporal evolution, is very informative and provides a powerful framework for understanding the flow kinematics of complex fluids:

(i) The velocity maps, as those shown in Fig. 3, provide useful information on the dependence of the velocity v along the vorticity direction $\mathbf{e}_z$. These maps are very useful for (i) assessing the presence of multi-dimensional flows arising, for example, from hydrodynamic or elastic instabilities, and (ii) studying their kinematics under shear.[46,49]

(ii) The use of the height-averaged velocity profiles enables the existence of multiple flow regimes along the gap to be detected. The transition from a flow band to another is generally accompanied by a pronounced slope change in the velocity profile.[50]

(iii) Note also that at the vicinity of the rotor and the stator, respectively, the contribution of the radial component v_r in eqn (4) vanishes, so that v is equal to the orthoradial velocity v_θ. This enables wall slippage to be assessed.

For information, the experimental velocity profiles were systematically compared with theoretical velocity profiles $v_{th}(r)$ obtained for a Newtonian fluid under no slip and purely orthoradial flow conditions. At a given macroscopic shear rate $\bar{\dot{\gamma}}$ (*i.e.*, at an imposed rotor rotation velocity Ω), $v_{th}(r)$ is defined as follows:

$$v_{th}(r) = \Omega\left(1 + \frac{r}{R_1}\right)\left[\frac{\left(\frac{R_2}{R_1 + r}\right)^2 - 1}{\left(\frac{R_2}{R_1}\right)^2 - 1}\right] \simeq \Omega\left(1 - \frac{r}{R_2}\right) \quad (5)$$

3 Results and discussion

3.1 Macroscale rheology coupled with optical flow visualization

The macroscale rheograms obtained for enzymatic and TEMPO NFC suspensions were complex and very sensitive to the experimental procedure. In Fig. 4 and 5, the macroscale rheograms obtained for the enzymatic and TEMPO NFC suspensions showed that these two suspensions behaved as thixotropic yield stress fluids. These suspensions exhibited a pronounced shear-thinning behavior at high shear rates $\left(50\ s^{-1} < \bar{\dot{\gamma}} < 1000\ s^{-1}\right)$. In this regime, the stress $\bar{\tau}$ was a power-law function of the applied shear rate $\bar{\dot{\gamma}}$, *i.e.*, $\bar{\tau} \propto \bar{\dot{\gamma}}^n$, with a macroscale power-law exponent n below 1 (n = 0.29 and 0.28 for the enzymatic and TEMPO suspensions shown in Fig. 4 and Fig. 5, respectively), whereas the suspensions exhibited an apparent yield stress $\bar{\tau}_0$ at low shear rates $\left(0.001\ s^{-1} < \bar{\dot{\gamma}} < 0.1\ s^{-1}\right)$.

For both types of suspensions, the flow curves obtained by sweeping up then down the shear rate $\bar{\dot{\gamma}}$ (Fig. 4a and 5a) were much more erratic and did not superimpose, particularly at low and intermediate shear rates $\left(0.001\ s^{-1} < \bar{\dot{\gamma}} < 10\ s^{-1}\right)$. In contrast, the flow curves obtained under sweeping down then up testing conditions (Fig. 4b and 5b) systematically displayed closed hysteresis loops within intermediate shear rates $\left(1\ s^{-1} < \bar{\dot{\gamma}} < 10\ s^{-1}\right)$ for enzymatic NFC suspensions and $\left(0.01\ s^{-1} < \bar{\dot{\gamma}} < 0.1\ s^{-1}\right)$ for TEMPO NFC suspensions, but were superimposed both at very low and high shear rates. Note also that the flow curves displayed several sudden drastic slope changes both during the upward and downward sweeps for all suspensions and under testing conditions.

Some of the 2D mesoscale optical observations of the suspensions that were obtained simultaneously to rheological measurements are visualized in Fig. 4 and 5. In particular, Fig. 4 showed that enzymatic NFC suspensions exhibited complex flocculated mesostructures. The evolution of these mesostructures could be related to some of the aforementioned complex variations of the flow curve. At low applied shear rates $\left(0.001\ s^{-1} < \bar{\dot{\gamma}} < 1\ s^{-1}\right)$, the obtained mesostructures were dependent on the sweeping direction. Indeed, under sweeping up then down testing conditions (Fig. 4a), the suspensions exhibited textures in the form of individual flocs ($<$100 μm, see Fig. 4a) during the upward sweep and textures in the form of floc chains ($\simeq$100–300 μm) during the downward sweep. These considerable mesostructural changes could explain the differences in yield stress levels that were recorded on the macroscopic flow curves. However, under sweeping down then up testing conditions (Fig. 4b) the suspensions displayed the same type of mesostructures both during the upward and downward sweeps. Within the intermediate shear rates $\left(1\ s^{-1} < \bar{\dot{\gamma}} < 10\ s^{-1}\right)$ and under all testing conditions, the viscosity plateaus were linked to drastic mesostructural changes. As previously reported by Saarikoski *et al.*[25] and Karppinen *et al.*[18] for enzymatic NFC suspensions or by Björkman[51] for pulp fiber suspensions, within this shear rate range the flow of the suspension in the gap was very complex: large clusters of flocs in the form of rolls and regions or voids free of fibers appeared. It is also important to note that under these conditions, any analysis of the macroscale rheograms in terms of continuous mechanisms should be considered cautiously because the size of the suspension heterogeneities can be of the same order of magnitude as the thickness of the sheared fluid. In the shear thinning branch of the flow curves $\left(10\ s^{-1} < \bar{\dot{\gamma}} < 1000\ s^{-1}\right)$, floc chains were totally disaggregated or split into individual and

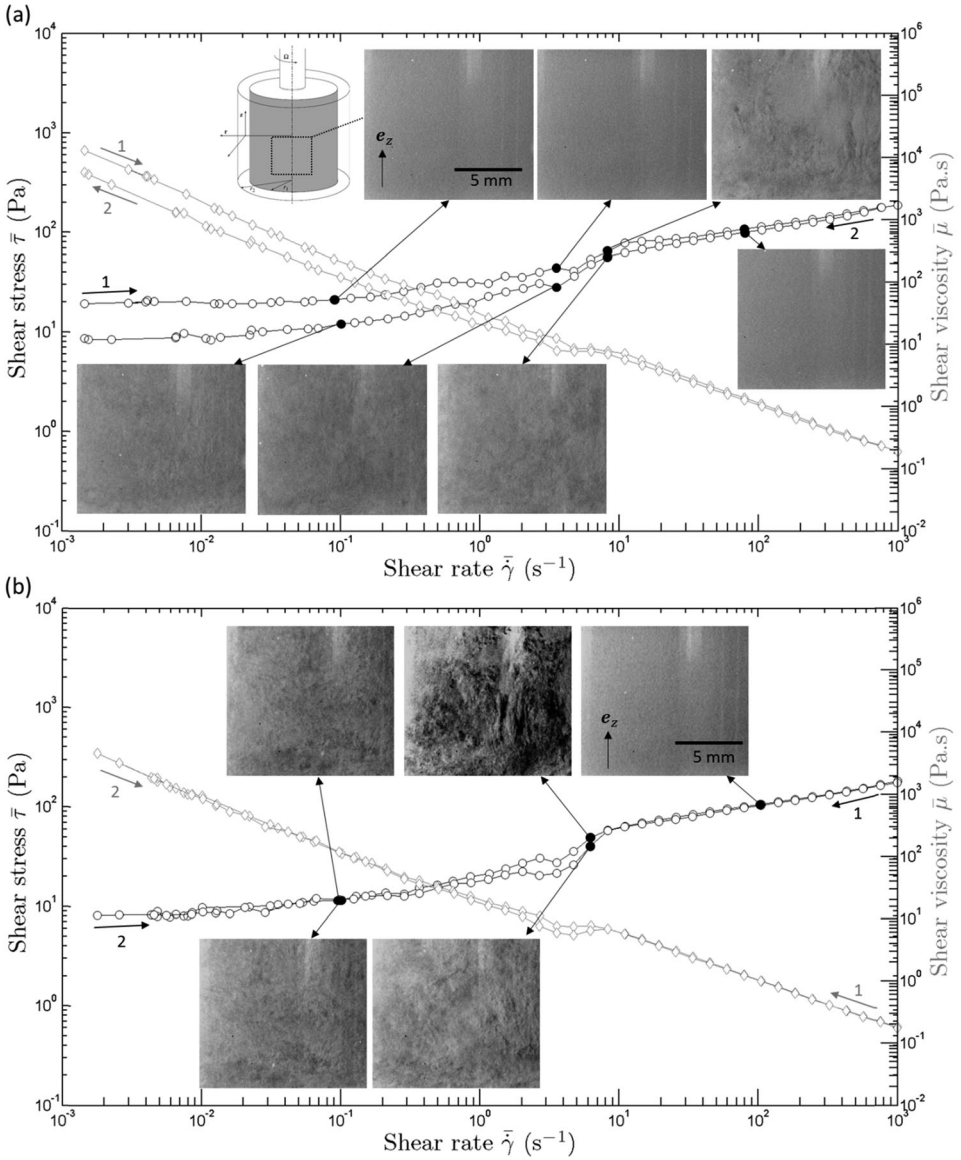

Fig. 4 Macroscale rheograms: macroscopic shear stress $\bar{\tau}$ (black circle symbols) and viscosity $\bar{\mu}$ (gray diamond symbols) as a function of the macroscopic shear rate $\dot{\bar{\gamma}}$ for a 2 wt% enzymatic NFC suspension obtained by first increasing the shear rate $\dot{\bar{\gamma}}$ from 0.001 to 1000 s^{-1} in 45 logarithmically spaced steps of duration δ_t = 50 s and then decreasing $\dot{\bar{\gamma}}$ over the same range (a), or *vice versa* (b). Insets: visualizations of the mesostructures of the suspensions at different macroscopic shear rates $\dot{\bar{\gamma}} = 0.1,\ 5,\ 8$ and 100 s^{-1}.

detached flocs (<100 μm). However, under all testing conditions, no drastic evolution in the floc size was clearly observed between the suspensions sheared at 100 s^{-1} and 1000 s^{-1}, so that the mechanisms involved in the shear thinning behavior may have occurred at a finer scale, *i.e.*, at the floc scale or even at the NFC scale. These last observations could explain why the stress levels recorded at high shear rates were very similar under all testing conditions.

The mesoscale structures of TEMPO NFC suspensions shown in Fig. 5 were very different from those of enzymatic suspensions. TEMPO NFC suspensions were nearly transparent, stable and non-flocculated either at rest or during shearing. Hence, the complexity of the macroscale rheograms shown in Fig. 5 cannot be explained using these 2D mesoscale observations, and may also be related to other potential sources commonly reported for other soft-glassy materials, *i.e.*, to mesoscale heterogeneous flow conditions associated with slippage at wall (stick-slip) and shear banding. For that purpose, a bulk analysis of kinematical fields is required (see next subsection).

3.2 Mesoscale rheology: description of the flow dynamics using rheo-USV measurements

Presumably because of the presence of flocs or aggregates (see Fig. 2a–c and Fig. 4a and b in the case of enzymatic NFC suspensions) and some rare macroscale fibers (see Fig. 2d–f in the case of TEMPO NFC suspensions), enzymatic and TEMPO NFC suspensions naturally scatter ultrasound when subjected

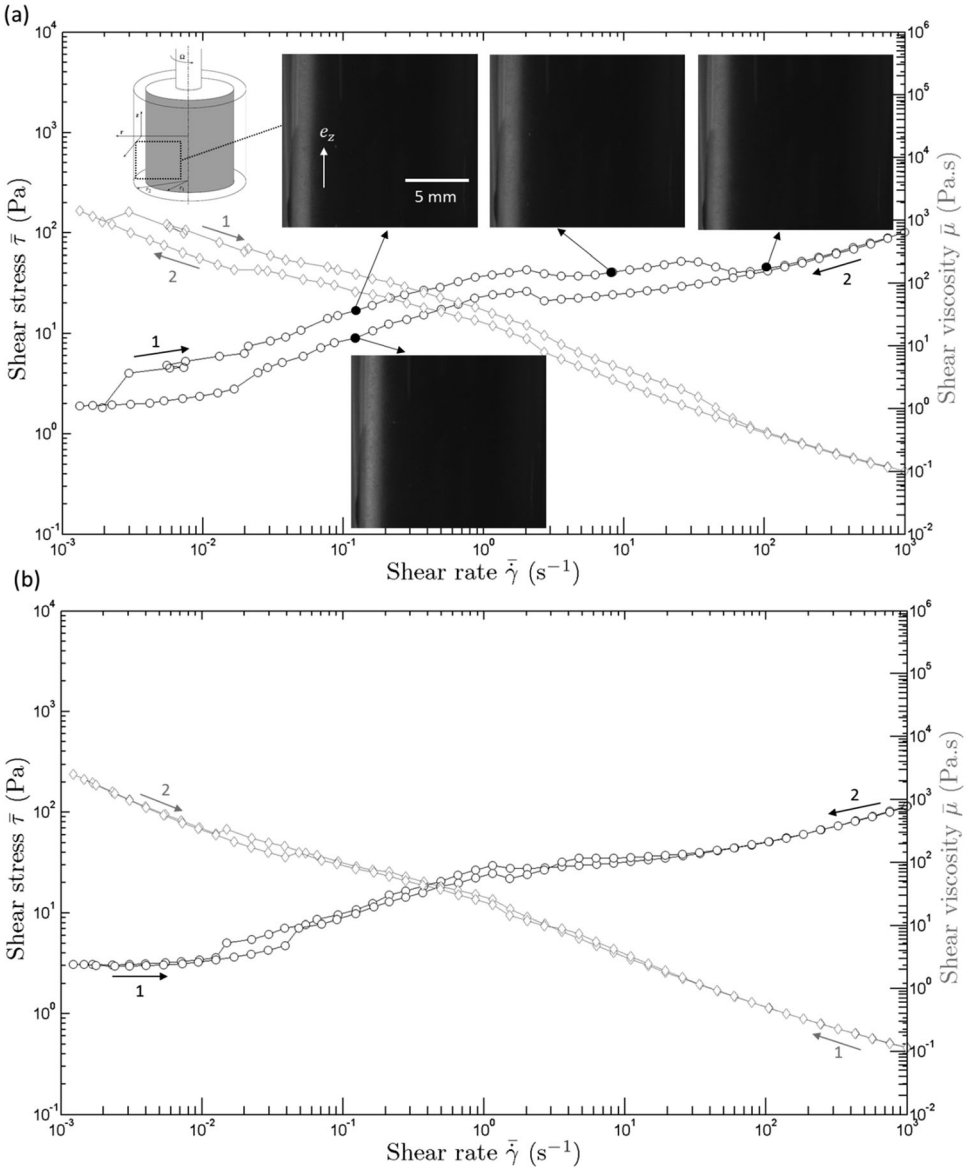

Fig. 5 Macroscale rheograms: macroscopic shear stress $\bar{\tau}$ (black circle symbols) and viscosity $\bar{\mu}$ (gray diamond symbols) as a function of the macroscopic shear rate $\dot{\bar{\gamma}}$ for a 1 wt% TEMPO NFC suspension, obtained by first increasing the shear rate $\dot{\bar{\gamma}}$ from 0.001 to 1000 s^{-1} in 45 logarithmically spaced steps of duration δ_t = 50 s and then decreasing $\dot{\bar{\gamma}}$ over the same range (a), or *vice versa* (b). Insets: visualizations of the mesostructures of the suspensions at different macroscopic shear rates $\dot{\bar{\gamma}} = 0.1,\ 5,\ 8$ and 100 s^{-1}.

to incident ultrasonic pulses. Hence, it was possible to use the USV technique directly for the NFC suspensions to obtain the 2D spatial and time-resolved characterization of the shear flow, *i.e.*, to acquire simultaneously both global rheological data and ultrasonic images of the phenomena that occurred inside the sheared suspensions (see the example in Fig. 3).

Fig. 6 and 7 give two significant examples of the typical information that was obtained by coupling standard rheometry with the USV technique during quick start-up shear tests from 0 to constant imposed shear rates for the enzymatic and TEMPO suspensions, respectively.

For both suspensions, graphs (a) in Fig. 6 and 7 showed that the time evolution of the macroscale shear stress $\bar{\tau}$ first exhibited a short and sharp increase up to a peak flow stress that was followed by a slower decrease down to a steady state regime over a few tens of seconds, a feature typical of thixotropic systems. The first regime was induced by the sudden shear rate jump from 0 to the imposed constant values. This behavior was probably related to the heterogeneous elastoviscoplastic deformation (see below) of the initially entangled nanostructure of the NFC suspensions. In the second stress regime, additional deformation mechanisms may have occurred so that the suspensions accommodated the imposed shear deformation: in the deformed zones of the suspensions (see Fig. 6c and 7c below and the related comments), NFCs may have progressively disentangled and deformed, which resulted in the formation of a new steady state structure where NFCs continuously lost and recreated their contacts. This phenomenon is illustrated in

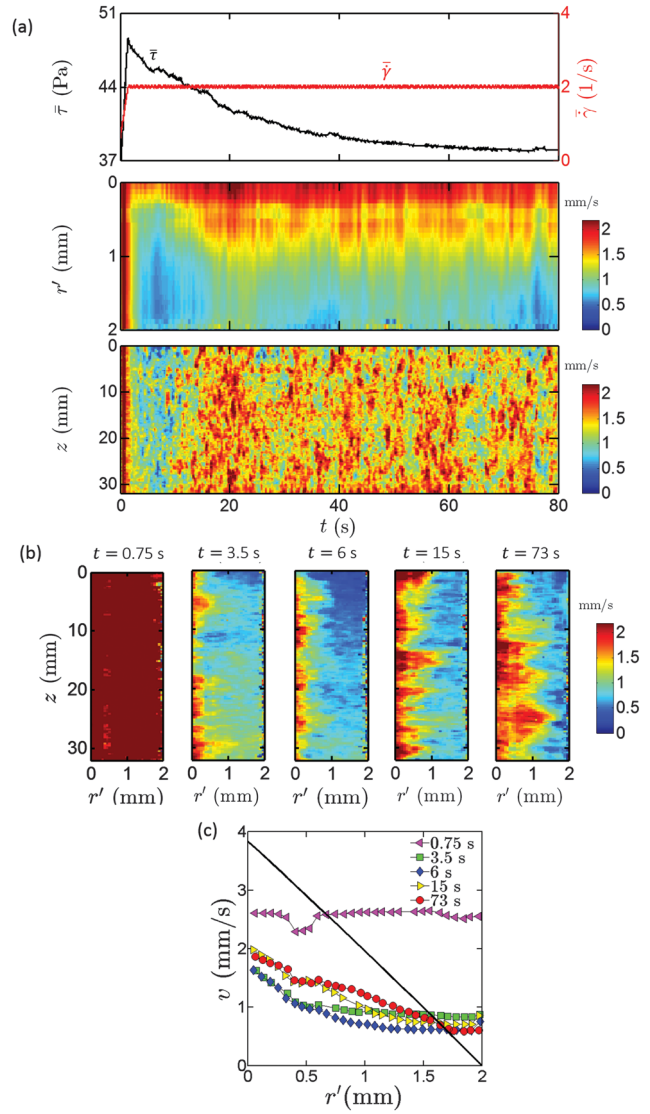

Fig. 6 Start-up of shear from 0 to 2 s^{-1} obtained for a 2 wt% enzymatic NFC suspension. (a) Time-evolution of the macroscale shear stress $\bar{\tau}$ (upper graph, black line) and the targeted macroscale shear rate $\dot{\bar{\gamma}}$ applied by the rheometer (upper graph, red line), and spatiotemporal diagrams of the height-averaged mesoscale velocity field $v(r',t)$ (middle graph) and of the local mesoscale velocity field $v(z,t)$ at r' = 0.4 mm. (b) Spatial velocity maps $v(r',z)$ taken at times t = 0.75 s, 3.5 s, 6 s, 15 s and 73 s. Each map corresponds to an average over 50 pulses sent every 0.5 ms. (c) Height-averaged velocity profiles obtained for the different times t as well as the theoretical profile (line in black) expected at 2 s^{-1} in the case of no slip 2D orthoradial flow.

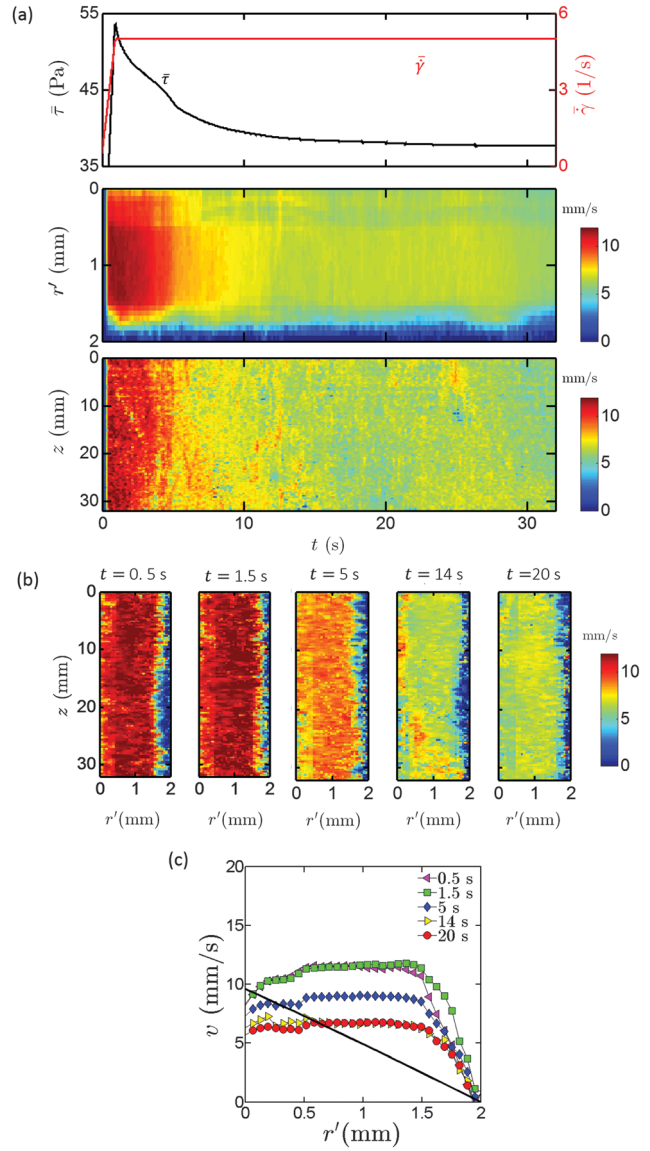

Fig. 7 Start-up of shear from 0 to 5 s^{-1} obtained for a 1 wt% TEMPO NFC suspension. (a) Time-evolution of the macroscale shear stress $\bar{\tau}$ (upper graph, black line) and the targeted macroscale shear rate $\dot{\bar{\gamma}}$ applied by the rheometer (upper graph, red line), and spatiotemporal diagrams of the height-averaged mesoscale velocity field $v(r',t)$ (middle graph) and of the local mesoscale velocity field $v(z,t)$ at r' = 0.4 mm. (b) Spatial velocity maps $v(r,z)$ taken at times t = 0.5 s, 1.5 s, 5 s, 14 s and 20 s. Each map corresponds to an average over 50 pulses sent every 0.5 ms. (c) Height-averaged velocity profiles obtained for the different times t as well as the theoretical profile (line in black) expected at 5 s^{-1} in the case of no slip 2D orthoradial flow.

graphs (c) in Fig. 6 and 7 where the r-profiles of the height-averaged value of the velocity field v evolved towards stabilized profiles after several tens of seconds.

For enzymatic NFC suspensions, the lower spatiotemporal diagram shown in Fig. 6a and the spatial velocity maps taken at different times shown in Fig. 6b were very erratic. The velocity v was heterogeneous over the entire height h of the Couette cell. These large spatial heterogeneities, the size of which was of the order of magnitude of the gap e, also evolved in time, which suggested the occurrence of complex 2D or 3D flow phenomena.

These bulk observations were in accordance with those made using the optical images shown in Section 3.1 and confirmed the presence of flocs having complex kinetics and kinematics under shear. These observations were also in agreement with surface and bulk observations made by Karppinen *et al.*[18] using an optical system and by Saarinen *et al.*[19] using optical coherence tomography, respectively. These results show once again that the dimensions of classical rheometers are probably not suitable for a relevant study of the bulk rheology of these unstable and

flocculated suspensions in the framework of continuum mechanics. However, these rheometers can be used to study shear flow phenomena occurring in confined geometries.

For TEMPO NFC suspensions, recorded spatiotemporal diagrams (Fig. 7a) and spatial velocity maps (Fig. 7b) were very different from those observed for enzymatic NFC suspensions (Fig. 6a and b). Indeed, even if the velocity field v was also heterogeneous, (i) its spatial and temporal variations were smoother and much less erratic, (ii) and this field was only weakly z-dependent. Thus, point (i) confirms the optical observations made in the previous section for TEMPO NFC suspensions: these suspensions did not exhibit mesoscale flocs at the micrometric scale. Point (ii) tends to prove that the flow of TEMPO NFC suspensions was mainly 2D and contained in the $(\mathbf{e}_r,\mathbf{e}_\theta)$ plane. Therefore, a deeper quantitative analysis of the rheometry experiments for TEMPO NFC suspensions can be more easily done compared to the case of enzymatic NFC suspensions. As shown in Section 3.4, more information on the bulk rheology of TEMPO NFC suspensions can also be extracted from the USV rheometry experiments.

Maps and profiles of the velocity field v (local or height-averaged) shown in Fig. 6b, c and 7b, c for enzymatic and TEMPO NFC suspensions, respectively, showed that in general, their flow was heterogenous and exhibited complex situations with the coexistence of multiple flow bands, and wall slippage. The complex flow patterns were far from those expected with a Newtonian fluid in a small-gap Couette rheometer (eqn (5)), as illustrated in Fig. 6c and 7c. For example, the mesoscale velocity profiles obtained for the enzymatic NFC suspension (Fig. 6c) revealed that a plug flow ($dv/dr \approx 0$) that nearly spanned over the entire gap probably occurred at the very beginning of the shear test. This phenomenon was accompanied by important wall slippage that could be observed both at the stator and the rotor. This phenomenon could also result in a progressive loading and a subsequent progressive strengthening or strain-hardening of the NFC network in the plug flow zone (see also our previous remark on the heterogeneous elastoviscoplastic deformation of the entangled NFC network before the peak stress). At t = 3.5 s, wall slippage increased on the rotor side ($r' = 0$) and two flow bands coexisted. A first flow band where $dv/dr \neq 0$ was formed near the rotor ($0 \leq r' \leq 0.4$ mm) and coexisted with a flow band where $dv/dr \approx 0$ near the stator (0.4 mm $\leq r' \leq$ 2 mm). Upon increasing the shearing time, the height-averaged velocity profiles revealed an increase of the width of the first flow band that progressively filled the entire gap. This transient behavior is reminiscent of the transient shear banding reported in carbopol microgels.[39,52] At the "steady state" ($t \geq 73$ s), in spite of the strong heterogeneity of the velocity map along the vertical direction (Fig. 6b), the suspension was roughly deformed in the entire gap, as shown by the last height-averaged velocity profile in Fig. 6c. Fig. 7c shows that the mesoscale velocity profiles of the TEMPO NFC suspension were also very complex. Before and after the stress peak at t = 1 s, the flow exhibited a large central flow band where $dv/dr \approx 0$ that coexisted with a second flow band where $dv/dr \neq 0$ next to the stator. At short times ($t < 1.5$ s), nearly perfect no slip boundary conditions were observed on both sides (rotor and stator), while in the longer run ($t > 1.5$ s), pronounced wall slippage was recorded near the rotor. The width of the flow band where $dv/dr \approx 0$ remained approximately constant and equal to 1.5 mm. A careful inspection of the velocity profiles (Fig. 7c) also revealed an even more striking phenomenon. At the beginning of the shear test, *i.e.*, from t = 0.5 s to t = 1.5 s, the velocity of the flow band where $dv/dr \approx 0$ passed through a maximum and reached values higher than the rotor velocity ($\approx$10 mm s^{-1}). This transient phenomenon has already been reported for other systems such as wormlike micellar solutions[49] or organogels.[50] The authors attributed it to the signature of a multi-dimensional flow induced by transient elastic-like effects,[49] suggesting that this phenomenon cannot be understood in the standard kinematic framework of the Couette flow, *i.e.*, 2D orthoradial flow $v_\theta(r)$. As inferred from eqn (4), a radial component v_r in the velocity field leads to an additional contribution $v_r/\tan\varphi$ to v. Note that since $\tan\varphi \approx 0.08$ for the present rheo-USV system, the effect of v_r on v was amplified by a factor of about 12. Hence, radial flow phenomena were also potentially at the origin of the aforementioned astonishing evolution of v.

These two examples show that rheo-USV provides a suitable and powerful framework for understanding the rheology of cellulose nanofibril suspensions. They emphasize the difficulty in properly assessing the "true" shear rate of these particular fiber suspensions from standard rheological measurements alone.

3.3 Multiscale rheology of TEMPO NFC suspensions

In this section, we describe in detail a set of results obtained for the unflocculated and stable TEMPO NFC suspensions, *i.e.*, suspensions for which a mesoscale analysis remained meaningful. More precisely, the complex macroscopic rheogram that was obtained for a 0.9 wt% TEMPO NFC suspension was studied simultaneously to the USV measurements. This is illustrated in Fig. 8 which shows the height-averaged steady-state velocity profiles obtained by sweeping up and then down the macroscopic shear rates ranging between 0.1 s^{-1} and 1000 s^{-1}.

All the plotted velocity profiles showed that the flow was inhomogeneous for both the upward and downward sweeps. Besides, the velocity profiles were also different showing that the flow was affected by the history of the macroscale applied shear rate $\bar{\dot{\gamma}}$. In addition, Fig. 8 also shows that wall slippage systematically occurred either on the rotor side or the stator side or on both sides. Lastly, two distinctive classes of flow bands also appeared while shearing the suspension: a first class where $dv/dr \approx 0$ and a second class where $dv/dr \neq 0$.

For the upward sweep and 0.1 s$^{-1} \leq \bar{\dot{\gamma}} \leq$ 1 s^{-1}, the suspension flow exhibited only two flow bands: a first flow band where $dv/dr \approx 0$ near the rotor (0 mm $\leq r' \leq$ 1.5 mm) and a second flow band where $dv/dr \neq 0$ located near the stator (1.5 mm $\leq r' \leq$ 2 mm). For 2 s$^{-1} \leq \bar{\dot{\gamma}} \leq$ 10 s^{-1}, the flow exhibited three bands: two flow bands where $dv/dr \neq 0$ near the rotor (0 mm $\leq r' \leq$ 0.3 mm) and the stator (1.4 mm $\leq r' \leq$ 2 mm) coexisted with a flow band where $dv/dr \approx 0$ (0.3 mm $\leq r' \leq$ 1.4 mm).

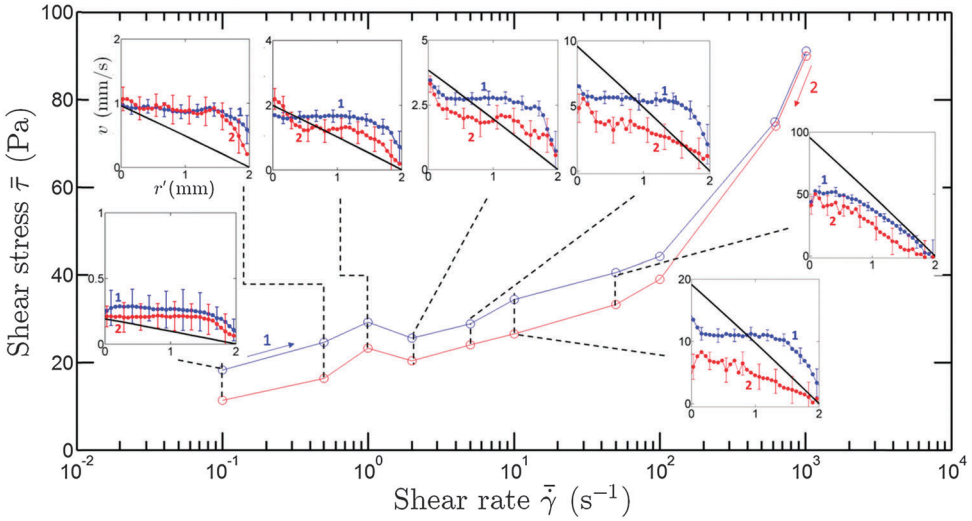

Fig. 8 Macroscale rheogram of a 0.9 wt% TEMPO NFC suspension obtained in a Couette rheometer first by sweeping up the shear rate $\bar{\dot{\gamma}}$ from 0.1 to 1000 s^{-1} in 10 steps of δ_t = 40 s. Insets: velocity profiles inside the gap of the Couette cell at $\bar{\dot{\gamma}} = 0.1,\ 0.5,\ 1,\ 2\ ,5,\ 10$ and 50 s^{-1} and 50 s^{-1} recorded during the upward (blue dots) and downward (red dots) sweeps after 50 s of shear. Number 1 denotes upward sweeps, whereas number 2 denotes downward sweeps.

At $\bar{\dot{\gamma}} = 50$ s^{-1}, the suspension displayed two flow bands having two different non-zero slopes: a first band close to the rotor (0 mm $\leq r' \leq$ 0.7 mm) and a second flow band close to the stator (0.7 mm $\leq r' \leq$ 2 mm). In summary, as the macroscale shear rate $\bar{\dot{\gamma}}$ was increased, the size of the flow band where dv/d$r \approx 0$ that was initially located near the rotor and then only in the middle of the gap progressively disappeared for the highest macroscale shear rates $\bar{\dot{\gamma}}$ (see Table 1). These evolutions of the mesoscale velocity maps also corresponded to a complex evolution of the macroscale stress as shown in Fig. 8. For instance, the macroscale shear stress reached a local maximum at a macroscale shear rate $\bar{\dot{\gamma}} = 1$ s^{-1} that was followed by a drop at $\bar{\dot{\gamma}} = 2$ s^{-1}. This behavior corresponded to a transition between a flow that exhibited two bands towards a flow where three bands coexisted (see also Table 1).

Table 1 Summary of the macro and mesoscale data obtained by sweeping up the macroscale shear rate $\bar{\dot{\gamma}}$ from 0.1 to 1000 s^{-1}

Macroscale shear rate $\bar{\dot{\gamma}}$ (s^{-1})	Total number of bands	Thickness of the bands (mm)	Mesoscale shear rate $\dot{\gamma}$ (s^{-1})
0.1	2	0 mm $\leq r' \leq$ 1.6 mm	0.04
		1.6 mm $\leq r' \leq$ 2 mm	0.3
0.5	2	0 mm $\leq r' \leq$ 1.6 mm	0.08
		1.6 mm $\leq r' \leq$ 2 mm	0.7
1	2	0 mm $\leq r' \leq$ 1.5 mm	0.1
		1.5 mm $\leq r' \leq$ 2 mm	1.7
2	3	0 mm $\leq r' \leq$ 0.3 mm	2.7
		0.3 mm $\leq r' \leq$ 1.6 mm	0.3
		1.6 mm $\leq r' \leq$ 2 mm	6.6
5	3	0 mm $\leq r' \leq$ 0.3 mm	3.5
		0.3 mm $\leq r' \leq$ 1.6 mm	0.5
		1.6 mm $\leq r' \leq$ 2 mm	8.4
10	3	0 mm $\leq r' \leq$ 0.2 mm	18
		0.2 mm $\leq r' \leq$ 1.4 mm	0.9
		1.4 mm $\leq r' \leq$ 2 mm	32.1
50	2	0 mm $\leq r' \leq$ 0.7 mm	12.2
		0.7 mm $\leq r' \leq$ 2 mm	24.2

For the downward sweep, heterogeneous velocity profiles were also recorded. The situation seems to be even more complicated than for the upward sweep. For instance, at $\bar{\dot{\gamma}} = 50$ s^{-1}, a bumpy velocity profile was recorded. As the shear rate was further decreased, the strong heterogeneity of the velocity profile persisted. The velocity profiles revealed a progressive transition between flow regimes with noisy, bumpy velocity profiles for 0.5 s^{-1} $\leq \bar{\dot{\gamma}} \leq$ 50 s^{-1} to a situation where only two bands coexisted at $\bar{\dot{\gamma}} = 0.1$ s^{-1}: a narrow flow band where dv/d$r \neq 0$ near the stator (1.7 mm $\leq r' \leq$ 2 mm) and a large band where dv/d$r \approx 0$ near the rotor (0 mm $\leq r' \leq$ 1.7 mm). While decreasing the shear rate $\bar{\dot{\gamma}}$ in a range varying from 10 s^{-1} to 0.5 s^{-1}, a flow band where dv/d$r \approx 0$ progressively enlarged and connected in the middle of the Couette cell (0.5 mm $\leq r' \leq$ 1.7 mm). This transition was accompanied by a non-monotonic evolution of the macroscale shear stress. In particular, as for the upward sweep, a local maximum in the macroscale stress was observed at $\bar{\dot{\gamma}} = 1$ s^{-1}. Here it corresponded to a situation where the number of bands in the velocity profile progressively turned from three to two at $\bar{\dot{\gamma}} = 0.1$ s^{-1} (see Fig. 8 and Table 2).

3.4 Discussion

For TEMPO NFC suspensions, the use of the USV measurements enabled a link between the events from the macroscale flow curves and the mesoscale flow kinematics to be quantitatively established. These USV measurements showed that the

Table 2 Summary of the macro and mesoscale data obtained by sweeping down the macroscale shear rate $\bar{\dot{\gamma}}$ from 1000 to 0.1 s^{-1}

Macroscale shear rate $\bar{\dot{\gamma}}$ (s^{-1})	Total number of bands	Thickness of the bands (mm)	Mesoscale shear rate $\dot{\gamma}$ (s^{-1})
50	2	0 mm $\leq r' \leq$ 0.4 mm	11.3
		0.4 mm $\leq r' \leq$ 2 mm	30.1
10	1	0 mm $\leq r' \leq$ 2 mm	4
5	3	0 mm $\leq r' \leq$ 0.3 mm	9.5
		0.3 mm $\leq r' \leq$ 0.9 mm	3.7
		0.9 mm $\leq r' \leq$ 2 mm	2.4
2	3	0 mm $\leq r' \leq$ 0.2 mm	5.3
		0.2 mm $\leq r' \leq$ 1.4 mm	0.4
		1.4 mm $\leq r' \leq$ 2 mm	2.1
1	3	0 mm $\leq r' \leq$ 0.3 mm	3.1
		0.3 mm $\leq r' \leq$ 1.4 mm	0.2
		1.4 mm $\leq r' \leq$ 2 mm	1.7
0.5	3	0 mm $\leq r' \leq$ 0.3 mm	1.1
		0.3 mm $\leq r' \leq$ 1.5 mm	0.1
		1.5 mm $\leq r' \leq$ 2 mm	1.4
0.1	2	0 mm $\leq r' \leq$ 1.7 mm	0.007
		1.7 mm $\leq r' \leq$ 2 mm	0.3

flow was affected by the presence of wall slippage and multiple flow bands that evolved with the macroscopic shear rate. In addition, the optical observations shown in Section 3.1 did not reveal clear evidence of mesostructural changes in the TEMPO NFC suspensions. Hence, the phenomena leading to both wall slippage and the coexistence of multiple flow bands may occur at a lower scale, *i.e.*, at the microscale and may be related to microstructural changes in the network of NFCs, deformation of NFCs and/or concentration gradients within the gap.

The phenomenon of wall slippage has often been reported for a variety of systems including pastes, colloids and polymers.[38,45,53] This phenomenon is affected by the geometry (*e.g.* surface roughness) and the physico-chemical nature of the solid–fluid interface. However, the origin of this phenomenon at finer scales and its effects on the flow kinematics and the microstructures still remain poorly understood. In the case of heterogeneous and polydisperse systems, wall slippage is often considered as resulting from a natural particle depletion phenomenon,[19,53] *i.e.*, a sudden decrease in the concentration of elements near the rheometer walls. The depletion of the particles can be enhanced by the flow, which can induce a migration from the high-shear regions towards the low-shear regions. For the negatively charged TEMPO NFC suspensions, the use of positively charged solid interfaces (for example, the rheometer walls in this study) would probably enhance the adhesion, leading to a decrease of the wall depletion effects.

The difference in macroscopic stress levels recorded during the upward and downward sweeps (see Fig. 8) could be attributed to the coexistence of multiple flow bands having different kinetics and kinematics under shear. These types of heterogeneous velocity profiles have already been reported for a variety of soft systems ranging from surfactants, wormlike micelles,[50,54,55] organogels,[49] triblock copolymers[56] and clay suspensions.[57] By varying the sweep rates, the authors[39,40] have shown that the kinetics of the multiple mesoscale bands could be interpreted using a characteristic time resulting from the competition between physical aging (restructuring mechanisms) and shear rejuvenation (structure breakup).

As pointed out in Section 2.3.2, the rheo-USV setup provides a rich but incomplete description of the flow dynamics. Note that similar problems also occur using other advanced velocimetry techniques such as those based on Magnetic Resonance Imaging (MRI). Thus, to further analyze the rheology of TEMPO NFC suspensions, several assumptions on the flow in the Couette cell must be considered:

– For instance, it may reasonably be assumed that the flow kinematics were independent of the vorticity direction $\mathbf{e}_z$, *i.e.*, the TEMPO NFC suspensions did not exhibit any vertical recirculating flows ($v_z \approx 0$). This assumption is supported by the visualizations shown in Fig. 5 which tend to prove that the suspension flow was mainly contained in the ($\mathbf{e}_r$,$\mathbf{e}_\theta$) plane, as the macroscale fibers that were present in the TEMPO NFC suspensions did not display any noticeable vertical displacements under shear.

– Further, the derivative of the velocity v with respect to r can be expressed from eqn (4) as follows:

$$\frac{dv}{dr} = \frac{dv_\theta}{dr} + \frac{1}{\tan(\varphi)}\frac{dv_r}{dr}. \quad (6)$$

Then, two typical flow situations corresponding to $dv/dr \approx 0$ and $dv/dr \neq 0$ can be considered. As shown in the velocity profiles of Fig. 8, flow situations where $dv/dr \approx 0$ occurred within bands of several hundred microns in width. In these bands, it seems unlikely that the two terms of eqn (6) systematically balance each other out. Presumably in these flow situations $dv_r/dr \approx 0$ and $dv_\theta/dr \approx 0$, *i.e.*, the radial and orthoradial components of the velocity are constant over the gap width. However, in the absence of any recirculation phenomena, a flow condition where the radial component v_r is a non-zero constant across the gap is unphysical (the fluid cannot go out of the measuring cell). Note also that in these ''plug-like'' flow bands, v_θ is probably constant, thus, meaning that the suspension is actually very weakly sheared. Similarly, a flow where $dv/dr \neq 0$ leads to $dv_r/dr \neq 0$ and $dv_\theta/dr \neq 0$: in this case the suspension is much more deformed.

Bearing in mind the aforementioned remarks, Fig. 8 shows that the plug-like flow zones where $dv/dr \approx 0$ were located close to the rotor, whereas the deformed zones where $dv/dr \neq 0$ were surprisingly located near the stator. Taking into account the slight decrease (15% in our case) in the shear stress τ along the rheometer radius r from the rotor to the stator:

$$\tau(r) = \frac{\Gamma}{2\pi h r^2}, \quad (7)$$

it is worth noting that the deformed bands appeared in the lowest shear stress zones. For simpler yield stress fluids, the opposite situation has usually been reported, in general, deformed zones are observed near the rotor, *i.e.*, in the highest

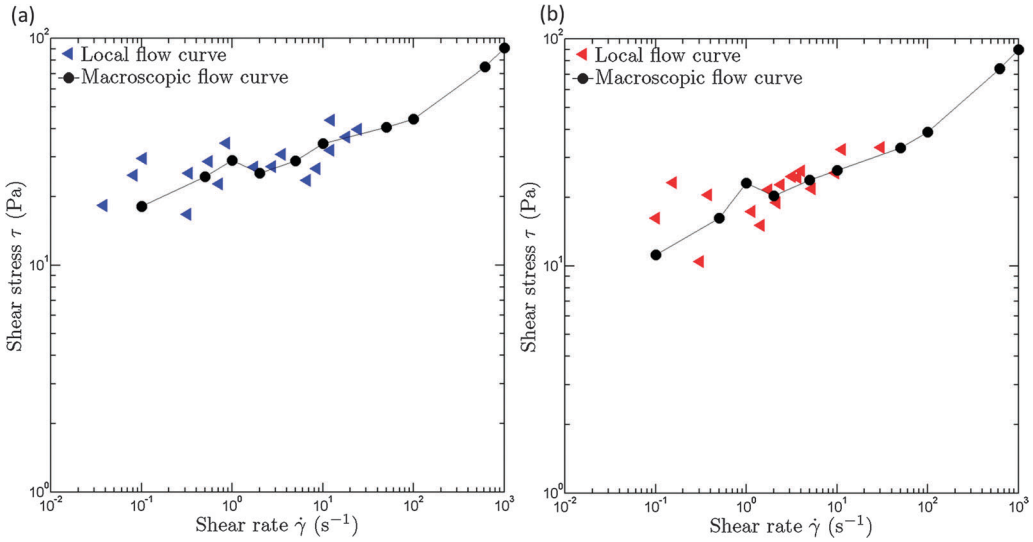

Fig. 9 Flow curves showing the evolution of the mesoscale shear stress τ (calculated from eqn (7)) as a function of the mesoscale shear rate $\dot{\gamma}$ given in Tables 1 and 2: (a) results obtained for upward sweep of the macroscale shear rate (blue dots) and (b) results obtained for downward sweep (red dots). The macroscale flow curve is shown for comparison (black curve).

shear stress zones. As for the studied TEMPO NFC suspensions, Saarinen *et al.*[19] have also reported for enzymatic NFC suspensions the presence of deformed bands in the lowest shear stress zone. The authors associated this phenomenon with wall depletion, *i.e.*, a drop in the NFC concentration profile near the stator. Here for the stable and unflocculated TEMPO NFC suspensions, a similar particle depletion phenomenon may have occurred. This phenomenon could be related to a potential strain-induced contraction of the NFC network. This contraction/consolidation could induce a migration of the fluid phase (water) towards regions where the stress is lower, *i.e.*, close to the stator. This scenario would have to be confirmed by additional investigations.

Fig. 8 also shows that the transition from a solid to a liquid-like behavior of the studied TEMPO NFC suspensions was heterogeneous as plug-flow zones and much more deformed zones coexisted over a wide range of the macroscopic shear rate. We note also that the size of these zones evolved as a function of the macroscopic shear rate. Therefore, we propose to interpret the evolution of the shear stress as a function of the shear rate during the upward sweep in terms of suspension fluidization involving several deformation mechanisms at the microscale. The first mechanism could be a progressive strengthening or strain-hardening of the NFC network in plug-like flow zones. In the insets of Fig. 8 for shear rates $\bar{\dot{\gamma}} < 1\ s^{-1}$, note that the width of the plug-like flow zones almost remained the same. However, from 0.1 to 1 s^{-1}, the induced deformation in these zones slightly increased. If the plug like flow zones could sustain this increase in shear, a potential reason for that could be that the suspension strengthened because of a potential strain hardening elastoviscoplastic behavior of the entangled NFC network (see also our previous remark in Section 3.2). Then, while increasing the shear rate, this mechanism could be followed by the fracture and the progressive disentanglement of the NFC network (for instance, see the drops in the macroscale stress in Fig. 5b and 8 for $\bar{\dot{\gamma}} > 1\ s^{-1}$). At the highest shear rates, shear-induced alignment and stretching of NFC slender particles could eventually occur (predominance of viscous effects on restructuring effects).

During the downward sweep, the suspension did not remain fluidized as shown by the progressive and successive formation of plug-like flow bands, which spanned nearly completely over the Couette cell width (see the velocity profiles in Fig. 8). This phenomenon may be related to fast restructuring phenomena, *i.e.*, the fast formation of a network of colloidal interactions between NFCs, dominating the viscous effects[40] and leading to plug-like flow bands.

Even if the radial component v_r cannot be assessed using the rheo-USV nor the optical observations, we make the assumption that this component was small for the steady-state velocity profiles that are shown in Fig. 8. Thus, a rough estimate of the mesoscale shear rate $\dot{\gamma}(r)$ within each flow bands was obtained from the height-averaged velocity profile $v(r)$ as follows:

$$\dot{\gamma}(r) \approx \frac{v(r)}{r} - \frac{\mathrm{d}v(r)}{\mathrm{d}r}. \quad (8)$$

The estimated values of the mean mesoscale shear rate $\dot{\gamma}$ within each flow bands, and their associated mesoscale mean shear stress τ (calculated from eqn (7)), are shown in the rheograms of Fig. 9. This figure shows that the as-estimated mesoscale flow curves were multivalued, *i.e.*, a mesoscale shear stress could correspond to several mesoscale shear rates. The difference between the shear rates in each band (Fig. 8 and 9 and Tables 1 and 2) was probably responsible for this phenomenon as each band did not reach the same level of shear strain during the sweep duration, and presumably did not acquire a similar microstructure. However, these mesoscale flow curves tend to show that the TEMPO NFC suspension behaved as a thixotropic

non-linear fluid having a steady state yield stress τ_0 close to 15–25 Pa, *i.e.*, a much higher yield stress value than the apparent yield stress $\bar{\tau}_0$ measured in the macroscale flow curves ($\bar{\tau}_0 \approx 3$ Pa). For pasty materials, the phenomenon of wall slip often leads to underestimate the macroscale shear stress, especially at low macroscale shear rates.[45,58]

4 Conclusion

The shear rheology of colloidal enzymatic and TEMPO NFC suspensions was experimentally investigated using a Couette rheometer equipped with (i) a transparent cell that enabled optical observations and (ii) an ultrasonic speckle velocimetry (USV) setup. The rheo-USV technique enabled an unprecedented description of the spatiotemporal evolution of mesoscale flow kinematics that occurred in shear rheometry experiments for suspensions of NFC in water.

Macroscale rheograms showed that both suspensions behaved as yield stress fluids that exhibited a pronounced shear-thinning behavior at high shear rates. These suspensions also showed significant history dependence (thixotropy), hysteresis loops during upward and downward sweeps and complex phenomena such as, for instance, abrupt shear stress decrease as the shear rate was increased. All these phenomena suggested a strong coupling between flow and the structural properties of the studied NFC suspensions, but also inhomogeneous flow conditions.

The *in situ* optical observations revealed that the enzymatic NFC suspensions exhibited flocculated textures that evolved with the applied macroscopic shear rate and sweeping history. These observations, which are in accordance with previous studies,[18] also showed that some of the complex evolutions observed in the macroscale flow curves corresponded to erratic mesostructural changes. These mesostructural changes were not observed for TEMPO NFC suspensions.

For both types of suspensions, the spatiotemporal velocity diagrams and the velocity profiles obtained with the USV technique revealed that the flow was inhomogeneous for a wide range of applied shear rates and was affected by the presence of wall slip, multiple flow bands, as well as possibly two-dimensional or three-dimensional flows, resulting either from spatial heterogeneity of enzymatic NFC suspension or from elastic-like instabilities for TEMPO NFC suspensions as those encountered in other soft materials.[19,49–51,55,57]

For enzymatic NFC suspensions, the spatiotemporal velocity diagrams obtained using USV showed complex transient flow initiation and erratic events that occurred even if the macroscopic shear stress and the height-averaged velocity profile were apparently stabilized, suggesting that the steady-state flow conditions were not attained. These phenomena could result from the presence of floc chains or individual flocs whose sizes were of the order of the rheometer gap and were moving apart under shear. Hence, using these types of rheometers is certainly not suitable for a proper rheology analysis based on a standard continuum framework. Therefore, the rheological models that have been established for enzymatic NFC suspensions using these types of rheometers are questionable: the gap is not large enough to obtain relevant rheological bulk properties.

For TEMPO NFC suspensions, spatiotemporal velocity diagrams were very different from those of enzymatic NFC suspensions. Indeed, even if the velocity field was also heterogeneous, its spatial and temporal variations were smoother and much less erratic. This suggests that for TEMPO NFC suspensions the flow was only weakly z-dependent. Thus, it was possible to carry out a deeper analysis of the bulk kinematic fields, revealing that, in the investigated shear rate $\left(0.1\ \mathrm{s}^{-1} < \bar{\dot{\gamma}} < 50\ \mathrm{s}^{-1}\right)$, the flow was heterogeneous for both the upward and downward sweeps. The height-averaged velocity profiles showed that the flow was affected by wall slippage and the presence of multiple flow bands. Two distinctive classes of bands appeared while shearing the suspension: a first class where $\mathrm{d}v/\mathrm{d}r \approx 0$ and a second class where $\mathrm{d}v/\mathrm{d}r \neq 0$. The number and the kinetics of the different flow bands varied as a function of the applied macroscopic shear rate and the sweeping history.

In the probable absence of recirculating flows in the vorticity direction, the coexistence of these two types of bands could be related to a spatially heterogeneous transition from a solid-like to a liquid-like behavior of the TEMPO NFC suspensions. These phenomena could result from a competition between structuration phenomena that involve colloidal interactions between NFCs and that are predominant at low shear rates and destructuration phenomena that involve predominant viscous forces at higher shear rates.

This study provides a comprehensive framework for understanding the rheology of NFC suspensions. However, new experimental investigations should be performed to confirm that the flow is not affected by the presence of vertical recirculation phenomena, and that the contribution of the radial component is low compared to the orthoradial component of the velocity field. It would also be of great interest to complement this study by finer local measurements to observe potential changes in the suspension microstructures within the gap (migration, orientation, variations of volume fraction of NFC, deformation of NFC) to explain the origin of phenomena such as shear banding and wall slippage.

Acknowledgements

This research was made possible thanks to the facilities of the TekLiCell platform funded by the Région Rhône-Alpes (ERDF: European regional development fund). LGP2 and 3SR laboratories are parts of the LabEx Tec 21 (Investissements d'Avenir - grant agreement no. ANR-11-LABX-0030) and of the Énergies du Futur and PolyNat Carnot Institutes (Investissements d'Avenir – grant agreements no. ANR-11-CARN-007-01 and ANR-11-CARN-030-01). C. Perge, M.-A. Fardin and S. Manneville acknowledge funding from the Institut Universitaire de France and from the European Research Council under the European Union's Seventh Framework Programme no. FP7/2007-2013 and ERC Grant no. 258803. The authors gratefully acknowledge C. Sillard (LGP2) for the technical support in the use of the atomic force microscope.

References

1 L. J. Gibson, *J. R. Soc., Interface*, 2012, **9**, 2749–2766.
2 Q. Cheng and S. Wang, *Composites, Part A*, 2008, **39**, 1838–1843.
3 S. Tanpichai, F. Quero, M. Nogi, H. Yano, R. J. Young, T. Lindström, W. W. Sampson and S. J. Eichhorn, *Biomacromolecules*, 2012, **13**, 1340–1349.
4 R. Bardet and J. Bras, *Handbook of Green Materials*, World Scientific, 2014, vol. 5, pp. 207–232.
5 C. Aulin, G. Salazar-Alvarez and T. Lindström, *Nanoscale*, 2012, **4**, 6622–6628.
6 H. Sehaqui, N. Ezekiel Mushi, S. Morimune, M. Salajkova, T. Nishino and L. A. Berglund, *ACS Appl. Mater. Interfaces*, 2012, **4**, 1043–1049.
7 I. Siró and D. Plackett, *Cellulose*, 2010, **17**, 459–494.
8 A. Dufresne, *Nanocellulose: from nature to high performance tailored materials*, Walter de Gruyter, 2012.
9 T. Saito, T. Uematsu, S. Kimura, T. Enomae and A. Isogai, *Soft Matter*, 2011, **7**, 8804–8809.
10 M. Henriksson, G. Henriksson, L. A. Berglund and T. Lindström, *Eur. Polym. J.*, 2007, **43**, 3434–3441.
11 M. Pääkkö, M. Ankerfors, H. Kosonen, A. Nykänen, S. Ahola, M. Österberg, J. Ruokolainen, J. Laine, P. T. Larsson and O. Ikkala, *Biomacromolecules*, 2007, **8**, 1934–1941.
12 T. Saito, S. Kimura, Y. Nishiyama and A. Isogai, *Biomacromolecules*, 2007, **8**, 2485–2491.
13 A. Isogai, T. Saito and H. Fukuzumi, *Nanoscale*, 2011, **3**, 71–85.
14 T. Saito and A. Isogai, *Biomacromolecules*, 2004, **5**, 1983–1989.
15 Y. Qing, R. Sabo, J. Y. Zhu, U. Agarwal, Z. Cai and Y. Wu, *Carbohydr. Polym.*, 2013, **97**, 226–234.
16 K. L. Spence, R. A. Venditti, O. J. Rojas, Y. Habibi and J. J. Pawlak, *Cellulose*, 2011, **18**, 1097–1111.
17 G. Chinga-Carrasco, *Nanoscale Res. Lett.*, 2011, **6**, 1–7.
18 A. Karppinen, T. Saarinen, J. Salmela, A. Laukkanen, M. Nuopponen and J. Seppälä, *Cellulose*, 2012, **19**, 1807–1819.
19 T. Saarinen, S. Haavisto, A. Sorvari, J. Salmela and J. Seppälä, *Cellulose*, 2014, **21**, 1261–1275.
20 S. Fujisawa, Y. Okita, H. Fukuzumi, T. Saito and A. Isogai, *Carbohydr. Polym.*, 2011, **84**, 579–583.
21 M. Mohtaschemi, K. Dimic-Misic, A. Puisto, M. Korhonen, T. Maloney, J. Paltakari and M. J. Alava, *Cellulose*, 2014, **21**, 1305–1312.
22 C. Goussé, H. Chanzy, M. L. Cerrada and E. Fleury, *Polymer*, 2004, **45**, 1569–1575.
23 E. Lasseuguette, D. Roux and Y. Nishiyama, *Cellulose*, 2008, **15**, 425–433.
24 M. Iotti, Ø. W. Gregersen, S. Moe and M. Lenes, *J. Polym. Environ.*, 2010, **19**, 137–145.
25 E. Saarikoski, T. Saarinen, J. Salmela and J. Seppälä, *Cellulose*, 2012, 1–13.
26 M. Mohtaschemi, A. Sorvari, A. Puisto, M. Nuopponen, J. Seppälä and M. J. Alava, *Cellulose*, 2014, 1–13.
27 P. Chen, H. Yu, Y. Liu, W. Chen, X. Wang and M. Ouyang, *Cellulose*, 2013, **20**, 149–157.
28 H. Fukuzumi, R. Tanaka, T. Saito and A. Isogai, *Cellulose*, 2014, **21**, 1553–1559.
29 T. Saarinen, M. Lille and J. Seppälä, *Annu. Trans. Nord. Rheol. Soc.*, 2009, **17**, 121–128.
30 F. Martoïa, P. J. J. Dumont, L. Orgéas, M. N. Belgacem, C. Perge, M.-A. Fardin and S. Manneville, oral communication in GFR, Nantes, 2013.
31 P. Coussot, L. Tocquer, C. Lanos and G. Ovarlez, *J. Non-Newtonian Fluid Mech.*, 2009, **158**, 85–90.
32 S. Manneville, *Rheol. Acta*, 2008, **47**, 301–318.
33 P. C. F. Møller, S. Rodts, M. A. J. Michels and D. Bonn, *Phys. Rev. E: Stat., Nonlinear, Soft Matter Phys.*, 2008, **77**, 041507.
34 G. Ovarlez, S. Rodts, X. Chateau and P. Coussot, *Rheol. Acta*, 2009, **48**, 831–844.
35 G. Ovarlez, S. Cohen-Addad, K. Krishan, J. Goyon and P. Coussot, *J. Non-Newtonian Fluid Mech.*, 2013, **193**, 68–79.
36 P. Moller, A. Fall, V. Chikkadi, D. Derks and D. Bonn, *Philos. Trans. R. Soc., A*, 2009, **367**, 5139–5155.
37 T. Gibaud, D. Frelat and S. Manneville, *Soft Matter*, 2010, **6**, 3482–3488.
38 F. Pignon, A. Magnin and J.-M. Piau, *J. Rheol.*, 1996, **40**, 573–587.
39 T. Divoux, C. Barentin and S. Manneville, *Soft Matter*, 2011, **7**, 8409–8418.
40 T. Divoux, V. Grenard and S. Manneville, *Phys. Rev. Lett.*, 2013, **110**, 018304.
41 E. K. Hobbie, *Rheol. Acta*, 2010, **49**, 323–334.
42 P. Dumont, J.-P. Vassal, L. Orgéas, V. Michaud, D. Favier and J.-A. E. Manson, *Rheol. Acta*, 2007, **46**, 639–651.
43 R. J. Adrian, *Exp. Fluids*, 2005, **39**, 159–169.
44 P. T. Callaghan, *Rep. Prog. Phys.*, 1999, **62**, 599–670.
45 P. Coussot, *Rheometry of pastes, suspensions, and granular materials: applications in industry and environment*, John Wiley & Sons, 2005.
46 T. Gallot, C. Perge, V. Grenard, M.-A. Fardin, N. Taberlet and S. Manneville, *Rev. Sci. Instrum.*, 2013, **84**, 045107.
47 S. Manneville, L. Bécu and A. Colin, *Eur. Phys. J.: Appl. Phys.*, 2004, **28**, 361–373.
48 J. A. Pople, I. W. Hamley and G. P. Diakun, *Rev. Sci. Instrum.*, 1998, **69**, 3015–3021.
49 M. A. Fardin, C. Perge, N. Taberlet and S. Manneville, *Phys. Rev. E: Stat., Nonlinear, Soft Matter Phys.*, 2014, **89**, 011001.
50 P. Grondin, S. Manneville, J.-L. Pozzo and A. Colin, *Phys. Rev. E: Stat., Nonlinear, Soft Matter Phys.*, 2008, **77**, 011401.
51 U. Björkman, *Nord. Pulp Pap. Res. J.*, 2003, **18**, 32–37.
52 T. Divoux, D. Tamarii, C. Barentin, S. Teitel and S. Manneville, *Soft Matter*, 2012, **8**, 4151–4164.
53 H. A. Barnes, *J. Non-Newtonian Fluid Mech.*, 1995, **56**, 221–251.
54 J. P. Decruppe, O. Greffier, S. Manneville and S. Lerouge, *Phys. Rev. E: Stat., Nonlinear, Soft Matter Phys.*, 2006, **73**, 061509.
55 M. A. Fardin, C. Perge, N. Taberlet and S. Manneville, *Phys. Rev. E: Stat., Nonlinear, Soft Matter Phys.*, 2014, **89**, 011001(R).
56 S. Manneville, A. Colin, G. Waton and F. Schosseler, *Phys. Rev. E: Stat., Nonlinear, Soft Matter Phys.*, 2007, **75**, 061502.
57 T. Gibaud, C. Barentin, N. Taberlet and S. Manneville, *Soft Matter*, 2009, **5**, 3026–3037.
58 V. Bertola, F. Bertrand, H. Tabuteau, D. Bonn and P. Coussot, *J. Rheol.*, 2003, **47**, 1211–1226.